Contact-Resistive Sensing of Touch and Airflow Using A Rat Whisker

Anne En-Tzu Yang¹, Mitra J. Z. Hartmann², and Sarah Bergbreiter³

Abstract—Rats rely heavily on tactile information from their whiskers to acquire information about their surroundings. A whisker has no sensors along its length. Instead, mechanical deformation of the whisker is sensed via receptors at its base. The present study introduces a micro-sensor developed specifically to imitate the sensing of biological rat whiskers. The sensor responds to bending moments resulting from touch and/or airflow in two axes. The sensor was designed based on analytical models from cantilever beam theory, and the models were validated with finite-element analysis. Sensors were then fabricated using micro-milled molds and integrated into an Arduino-based circuit for simple signal acquisition. The present work begins to develop the technology to allow investigation of important engineering aspects of the rat vibrissal system at 1x scale. In addition to its potential use in novel engineering applications, the sensor could aid neuroscientists in their understanding of the rat vibrissal-trigeminal pathway.

I. INTRODUCTION

The rat vibrissal (whisker) array (Fig. 1A) is an important model system for the neuroscience of touch and is in many ways analogous to the human hand. Behaviorally, rats use their whiskers for tactile exploration similar to the way in which humans use their hands. Physiologically, the neural pathways that carry information from the whiskers and hands share a similar structure. A major distinction between the two systems is that whiskers are mechanically simpler than hands, as they can be represented as cantilever beams with sensors located only at the base. In theory, this relative simplicity allows us to quantify the complete mechanical input to the whiskers during active sensing behaviors more easily than for hands. Quantifying the input (whisker mechanics) is necessary to reveal how the neurons process the mechanical signals to generate electrical output (action potentials).

However, it is not possible to directly measure the mechanics of the whiskers on the rat's face. Instead, researchers rely on image processing techniques and numerical modeling to infer and simulate whisker mechanics [10]. Simulations are often, though not always, limited to the quasi-static domain because whisker dynamics during texture exploration, noncontact whisking, and airflow sensing [18] are challenging to simulate [1][14][15][16]. Thus, the field of neuroscience would benefit from an engineered sensor to directly measure

*The present work was funded by National Science Foundation award BCS-1734981 to MJZH and SB.

signals from real, biological whiskers at 1x scale. Such a sensor could contribute to the validation of simulated quasistatic mechanics and improve our understanding of whisking dynamics.

Although a rat whisker can touch an object anywhere along its length, all information is transmitted to sensors (mechanoreceptors) located only at the whisker base [5]. Previous studies have shown that measurement of the lateral bending moments is sufficient in "pseudo-2D" [17] and crucial in 3D [9] to determine the location along the whisker at which contact is made. The taper [8] and elastic [13] properties of whiskers play critical roles in the efficiency of the mechanical information transfer process. In other words, biological whiskers have advantageous properties that are missing or difficult to control in artificial materials for robotic sensors. This study presents a sensor specifically tailored to measure signals at the base of biological whiskers. The soft, lightweight, and bio-compatible nature of the sensor also has potential to be used in devices such as flexible joysticks and other uses of electronic whiskers [6].

An initial version of the sensor was described as one of several applications in work that more generally focused on the development of mechanoreceptive skins [3]. The fabrication process in the present work is derived from the methods described in that paper. The primary contributions of the present work are an informed geometric design based on both analytical and finite element analysis (FEA) models, new material choices for fabrication, and new experimental results from touch and airflow sensing.

II. METHODS

The basic sensor design is shown in Fig. 1B. A whisker is inserted into a cylindrical central pillar made from a conductive elastomer. As the whisker is bent, the pillar contacts surrounding pads (made of the same elastomer), forming a conductive pathway between the pillar and those pads. To obtain a usable signal from this sensor, both the geometry and material choices are important, as described below.

A. Materials Preparation

Two composite materials were used in the present study:

Material I: consistent with previous work [3], Material I used polydimethylsiloxane (PDMS) (Sylgard 184, Dow Corning) as the base dielectric layer and carbon nano-tubes (CNT) (Multi Walled Carbon Nanotubes, SKU 030103, outer diameter: 10-20 nm; length: 10-30 μm) mixed with PDMS as the material for conductive

 $^{^1}$ Department of Mechanical Engineering, Northwestern University, Evanston IL 60208 USA <code>ay@u.northwestern.edu</code>

² Departments of Mechanical Engineering and Biomedical Engineering, Northwestern University, Evanston IL 60208 USA hartmann@northwestern.edu

³ Department of Mechanical Engineering and Institute for Systems Research, University of Maryland, College Park MD 20742 USA sarahb@isr.umd.edu

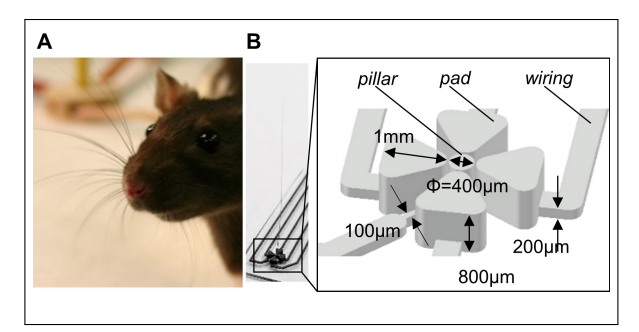


Fig. 1. (A) A photograph of a rat and its whiskers. (B) A photograph of the sensor and an expanded schematic of the sensing region. The dimensions and features in the sensing region are labeled. The central pillar is $400 \ \mu m$ in diameter. Each of the surrounding pads has an approximately triangular cross-section (a "wedge") $1 \ mm$ across.

features. Materials were mixed by a speed mixer (DAC 150, FlackTek Inc.) at 2000 *rpm* for 90 *s*.

 Material II: Inspired by a material modification reported in other studies [4][12], we followed the approach of Chen et al. [4] to determine if adding sugar enhance the surface conductivity of the CNT-PDMS composite. Powdered sugar was selected for its grain size (<10 μm), suitable for homogeneous distribution. To avoid the anti-caking agents typically added to commercially available powdered sugar, we ground cane sugar into powder using a mortar and pestle.

B. Mechanical Simulation of Sensor Deformation

To customize the sensor for contact-resistive sensing, there are three important design features—one "pillar" to which the rat whisker is attached, three or four "pads" surrounding the pillar, and the gap between the pillar and each pad. The minimum width of the pillar is constrained by the tool diameter of the micro-mill. The pillar size also needs to be sufficient to hold a typical whisker, with a length of \sim 35 mm and a diameter of \sim 150 μm . The gap widths are determined by the repeatability of the micro-mill. The geometry of the pads is less constrained, but still must be larger than the smallest tool diameter used. We used beam bending theory along with FEA simulations to guide the design for the pads. A design is considered advantageous if it results in greater reaction forces between contacting features. In the computational simulation performed in Abaqus, the two raw materials-PDMS and CNT-PDMS are defined to have a Young's modulus of 1.5 MPa and a Poisson's ratio of 0.49 [2][11].

C. Fabrication

The fabrication procedure follows that of Charalambides et al. [3] with some variations. A 0.25-inch thick acrylic sheet was milled using a bench-top micro-mill (Roland MDX-540SA) with end mills of diameters 406 and 100 μm . The milled features were then filled with one of the conductive materials described in section II-A. An automatic hydraulic heated laboratory press (model 3895, Carver, Inc.) applied a normal force of 500 kgf (4905 N) to ensure complete refill of the material. Excessive material was next removed using

a squeegee. The acrylic mold and the refilled conductive material were cured in a convection oven (Oster TSSTTV0001) at 200 °F (93.3 °C) for 30 minutes (including preheating time). Once the mold cooled down to room temperature, a dielectric PDMS layer was poured on top of the acrylic and conductive material. The mold carrying CNT-PDMS and PDMS was then placed into a vacuum chamber at 0.08 atm (-27.5 inHg) for 30 minutes. Finally, the entire workpiece was cured for a second time in the same convection oven at 200°F for 60 minutes (including preheating time). After curing and cooling, the sensors (sensing features and the base layer, at a maximum depth of $800~\mu m$) were manually peeled away to detach them from the mold.

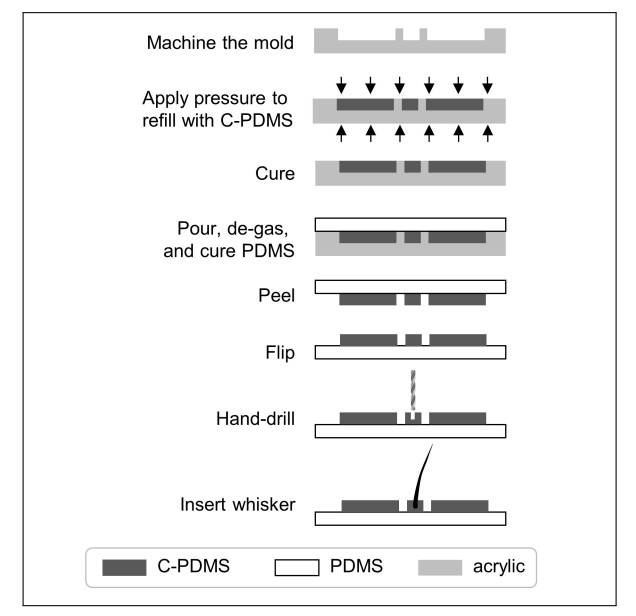


Fig. 2. Fabrication flow chart for the sensor. The number of steps remains the same regardless of the number of sensors in the array.

D. Whisker Attachment

It was important to avoid glue when inserting the whisker into the central pillar, because it would have spread to create an insulation layer on the surface of the conductive material. We therefore used a press-fit approach. A micro drill-bit 150- μm in diameter (high-speed steel micro-size drill bit, 0.0059", McMaster-Carr) was inserted by hand through the center of the length of the pillar, starting from its top surface. The drill-bit was removed from the pillar when the hand-drilling was complete. A large whisker was then obtained from a ~ 3 month female Long Evans rat euthanized in an unrelated experiment. The whisker was inserted into the drilled clearance. The whisker remained fixed within the sensor because the base diameter of the whisker was slightly larger than that of the drill-bit.

E. Voltage Divider for Contact Resistive Sensing

The sensor transduction is based on contact-resistive sensing, which simplifies the electronic interface required to pick up signals when features come into contact. The pillar is connected to a 5 V supply (V_{in}). The connection to each pad

yields one voltage output (V_{out}) . The resistance between the pillar and each pad is denoted as R_1 . In addition, a reference resistor, R_2 , is connected between voltage output (V_{out}) and ground (GND). Therefore, the voltage output (V_{out}) from each pad and the supply voltage (V_{in}) have the following relationship:

$$V_{out} = \frac{R_2}{R_1 + R_2} V_{in} \tag{1}$$

When the sensor is at rest, the resistance (R_1) between the pillar and any of the pads is ∞ , resulting in an output voltage V_{out} of 0 V. As soon as a conductive path is formed between the pillar and a pad, the resistance (R_1) decreases to a finite value, and a non-zero V_{out} will be recorded. The value of the reference resistor (R_2) is selected to be similar to that of R_1 at an intermediate contact pressure, typically ~ 10 $k\Omega$, to achieve a good balance between noise and sensitivity. To record these voltage outputs, each V_{out} is connected to a computer through an ADC channel on an Arduino UNO microcontroller board.

III. RESULTS

A. Geometry and Contact Quality

We applied beam theory to determine the geometry that provides the largest reaction forces between parts of the sensor when the whisker is bent. Larger reaction forces will correspond to larger changes in the resistance of R_1 . A schematic for one sensing direction is shown in Fig. 3. In the left panel, two cantilever beams represent the center pillar and the surrounding pad spaced at a distance d. The two beams have area moments of inertia of I_1 and I_2 , respectively. Both beams have the same length, L, and the same Young's modulus, E. An external force P (equivalent to a bending moment of PL) is applied at the end of the first beam (the pillar). The first beam then deflects and touches the second beam, causing the second beam also to deflect.

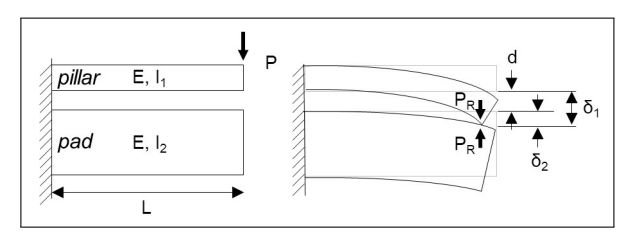


Fig. 3. A rotated view of the pillar and a pad, modeled as two cantilever beams of length L with moments of inertia I_1 and I_2 . The gap between the pillar and pad is d. The initial configuration before a load P is applied is illustrated on the left. The deflected condition under the applied load is shown on the right. The tips of the two beams deflect by δ_1 and δ_2 , respectively. The reaction force (P_R) between the two beams has the same magnitude but opposite signs.

Under the deflected condition, the reaction force to be maximized, P_R , has the same magnitude and opposite direction on each beam. As a result, the two beams experience forces of $(P - P_R)$ and P_R , respectively. From established beam bending equations [7], the tip deflections, δ_1 and δ_2 , are governed by P, P_R , L, E, I_1 , and I_2 :

$$\delta_1 = \frac{(P - P_R)L^3}{3EI_1}, \quad \delta_2 = \frac{P_R L^3}{3EI_2}$$
 (2)

To satisfy geometric compatibility conditions, as illustrated in the right panel of Fig. 3, the tip deflections, δ_1 and δ_2 , and the spacing d between the two beams must satisfy the following constraint:

$$\delta_1 = \delta_2 + d \tag{3}$$

Substituting (2) into (3), the equation can be rewritten as:

$$\frac{(P - P_R)}{3EI_1} = \frac{P_R}{3EI_2} + \frac{d}{L^3} \tag{4}$$

The last term in equation (4) is small compared to the other terms because the spacing between features d is much less than the length of beam L ($d \ll L$). The equation can thus be simplified as:

$$\frac{(P - P_R)}{I_1} = \frac{P_R}{I_2} \tag{5}$$

Finally, after rearranging equation (5), the force exerted by the pillar on a deflected pad is proportional to the external input force P:

$$P_R = \frac{I_2}{I_1 + I_2} P \tag{6}$$

Equation 6 indicates that when a pillar with moment of inertia I_1 is deflected by a given force, the reaction force will increase with the moment of inertia of the pad (I_2) . Therefore, a wedge geometry was chosen over a cylindrical geometry because it has a much larger moment of inertia. The width of the wedge increases radially from the pillar, which adds stability and prevents buckling (Fig. 1).

This theoretical derivation was validated with simulations in Abaqus (section II-B) that compared the effects of deflecting the pillar against a cylindrical and a wedge-shaped pad.

In the first set of simulations a 10 kPa pressure was applied to the top half of one side of the drilled hole in the pillar, driving the pillar towards the pad. The resultant elemental displacements are shown in Fig. 4B. The pillar displaced 26% more towards the cylinder (left) than towards the wedge (right). Moreover, the cylindrical pad displaced, but the wedge-shaped pad did not, indicating that a greater fraction of the work contributed to deformation of the wedge than of the cylinder.

A second set of simulations showed that for a displacement of 40 μm , the maximum resultant von Mises stress within the features was 76% greater in the wedge than in the cylinder, as demonstrated in Fig. 4C. These results are in line with the analytical derivation in section III-A.

B. Tactile Signal and Bending Moment

Two versions of sensors with three and four pads, respectively, were fabricated using *Material I*. Each version has its pros and cons.

Because the three-pad sensor is missing a pad on its fourth side, it cannot measure all 360° of possible whisker deflections. However, the absence of a fourth pad frees up space for wiring of the pillar. Because the wiring can be as wide as the pillar diameter, the entire sensor can be machined using the same tool.

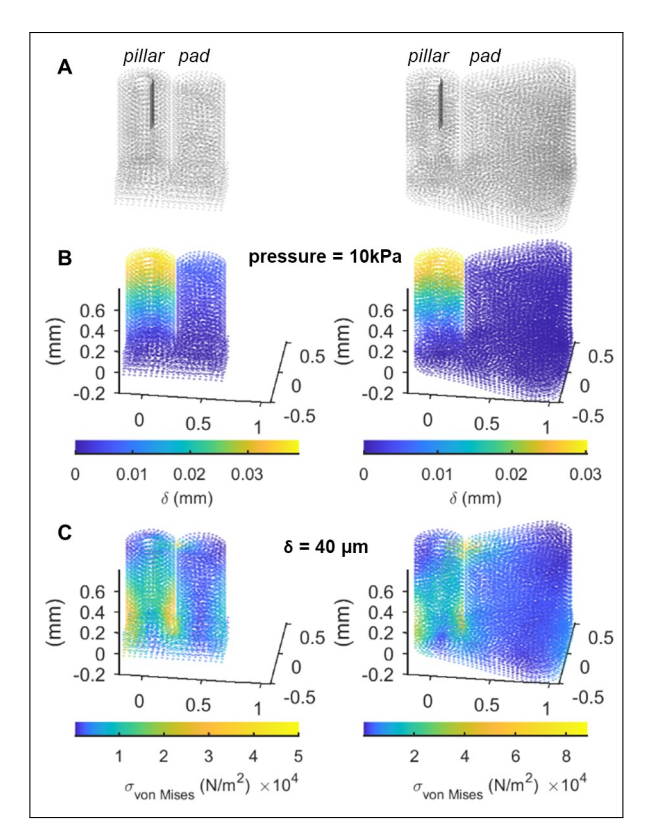


Fig. 4. Abaqus simulations were used to model the deformation and the stress generated when a cylindrical pillar deflects against a cylindrical pad (left column) and against a wedge-shaped pad (right column). (A) The Abaqus mesh representing the pillar and either a cylindrical pad (left) or a wedge shaped pad (right). The black shaded area represents a pressure acting on the inside surface of the hole, which deflects the pillar.(B) For a 10 kPa pressure, the maximum elemental displacements in the cylinder (left) ($\delta = 38.6 \ \mu m$) are greater than in the wedge (right) ($\delta = 30.6 \ \mu m$). (C) For a 40 μm displacement, the wedge produces larger maximum von Mises stress ($\sigma_{vonMises} = 88.4 \ kPa$) than does the cylinder ($\sigma_{vonMises} = 50.1 \ kPa$)

In contrast, the four-pad sensor can measure bending of the whisker in all directions, but the wiring space is severely reduced. The reduced wiring space necessitates a tool change during fabrication. Constrained by a 400- μ m tool diameter (ϕ_{tool}) and a 30 μ m gap size (d), two adjacent pads with an angular spacing of 90° have a maximum wiring clearance (D_{wire}) of 208 μ m, as calculated by equation (7). Hence, the wiring to the pillar must be machined by an end-mill with a 100- μ m diameter.

$$D_{wire} = \frac{\phi_{tool} + d}{\sin 45^{\circ}} - \phi_{tool} \tag{7}$$

Raw voltage signals (V_{out}) recorded from three-pad and four-pad sensors are displayed in Fig. 5. The whisker was manually deflected in one direction at a time, and data were recorded at 125 Hz. As expected, the largest value of V_{out} occurred for the pad towards which the whisker was deflected.

The noise floor for both sensor types can be seen in the voltage traces during times when the whisker is not deflected. Variability in V_{out} during deflections is likely to be primarily due to wobble in the manually-delivered stimulus.

Secondary signals are also present (e.g., orange under blue and blue under yellow), and appear to follow approximately the same time course as the primary signals. These secondary signals most likely occur because the manual stimulation caused the pillar to touch a second pad, however, further tests are required to rule out the possibility that the pillar deformed so as to contact a second pad, even given single-axis stimulation.

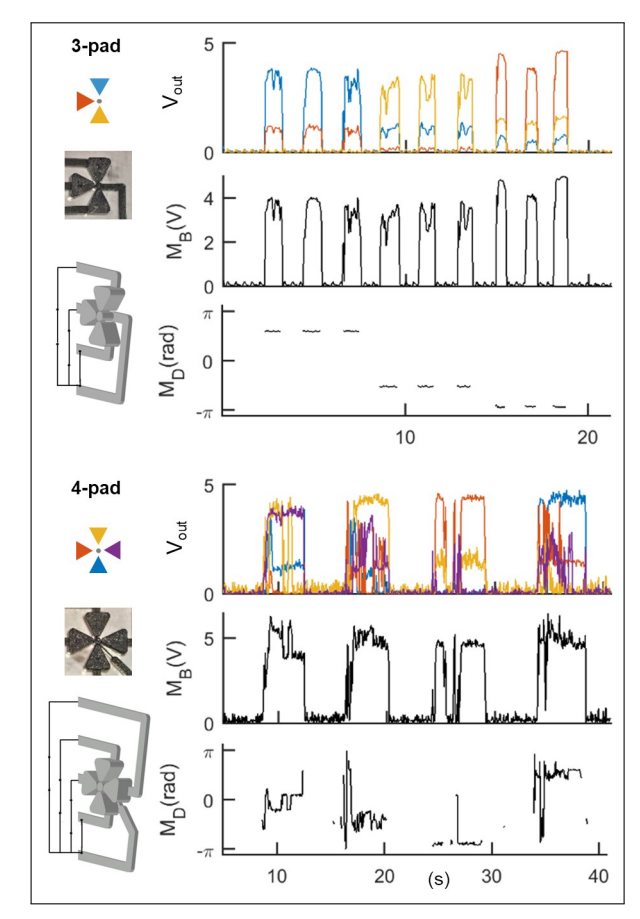


Fig. 5. Three- and four- pad versions of the sensor were fabricated and tested. During testing, the whisker was sequentially deflected in each direction. The top and bottom halves of the figure each include: a schematic that is color coded to match each pad to its corresponding voltage output, a top-down stereoscopic image, a wiring schematic, raw voltages (V_{out}) , and converted bending moment magnitude (M_B) and direction (M_D) . The MD plot omits values obtained when M_B was zero

The output voltages from the sensor can be converted into bending moment magnitude (M_B) and direction (M_D) by equations (8) and (9):

$$M_B = \sqrt{\sum_{i=1}^{N} V_{out,i}^2} \tag{8}$$

$$M_D = \arctan \frac{\sum_{i=1}^{N} V_{out,i} \sin \theta_i}{\sum_{i=1}^{N} V_{out,i} \cos \theta_i}$$
(9)

where N is the number of pads (either 3 or 4), and θ_i is the angular position of each pad $(90^{\circ}, 180^{\circ}, 270^{\circ}, 0^{\circ})$.

After conversion, M_B , retaining units of volts, is proportional to the magnitude of the bending moment. A calibration

curve is required to obtain the absolute value of the moments. The bending direction, M_D directly reflects the bending direction in radians. Results after conversion are shown as the black traces in the middle rows of Fig. 5.

In the three-pad results, the secondary signals are always smaller than the primary signals, regardless of deflection direction. After each deflection the resting voltages always return very close to zero, indicating the absence of obvious hysteresis. In addition, the M_D data unambiguously indicate the direction of bending stimuli and are consistent within each triplet sequence of deflections in a given direction.

Although V_{out} , M_B , and M_D signals from the four-pad sensor responded in similar manner to the three-pad sensor, the data are noisier (bottom half of Fig. 5). A likely cause for this additional noise is that the wiring to the four-pad sensor is much narrower than the wiring to the three-pad sensor. Structurally, the wiring serves as a spring constraining the pillar to the base layer. For the three-pad sensor, the trace connecting to the pillar is four times wider than the four-pad sensor, resulting in a relatively stiff pillar with a greater restoring force after deflection. The wiring to the pillar in the four-pad sensor is much narrower, resulting in less constraint on pillar motion and decreased sensor stability.

C. Response to Airflow

In a separate series of experiments, we investigated the sensors response to airflow. Because we expected the whiskers response to include dynamic oscillations, we increased the sampling rate to 1039 Hz. The data in this section were acquired using a sensor fabricated with *Material II*. Because these experiments focused only on quantifying bending magnitude, only one pad was tested. The reference resistance on the voltage divider was increased to 780 $k\Omega$ to improve sensitivity.

The setup and results are shown in Fig. 6. Airflow was generated from a compressed air source on a conventional lab bench (not shown in the picture). Air flowed through Tygon tubing with an inner diameter of 7.6 mm. The center of the cross-section of the tubing was fixed at a height of 22.5 mm above the base layer of the sensor and targeted the whisker approximately one-quarter of its length from its tip. At a distance of 7.5 cm from the tubing, the maximum airspeed was measured to be $10.0 \, m/s$ using a hot wire anemometer (Omega Engineering Inc.) when the room was at 24.1 °C.

In the first experiment, the sensor responded to constant airflow at two different distances. The outlet of the tubing was manually moved from afar to a distance of $\sim 3~cm$ in front of the whisker for about a minute (timed using the display on the Arduino board) and then moved away (in a "far-near-far" pattern). Fig. 6B shows signals from the sensor in a single, continuous trial. The voltage begins near zero (when the air source is far), remains at a constant offset value for a duration corresponding to the "near" duration, and then returns to zero afterwards.

The second experiment tested the sensor's response to airflow of varying speeds. Throughout this trial, the tubing was fixed at a horizontal distance of 22 mm from the whisker.

Airflow was manually adjusted to gradually increase from zero to the maximum speed, held at the maximum, and then decreased back to zero (in a "up-hold-down" pattern). Voltage readings from a single, continuous trial are depicted in Fig. 6C. The voltage appeared to be related to the adjustments in airspeed. During the ramp-up phase, timed on the Arduino display between 5-17 *s*, the sensor voltage exhibited a steep and noisy increase before more steadily increasing with airspeed. This sensor behavior suggests the presence of a detection threshold. Similarly, as airflow was decreased, between 22-34 *s*, the voltage exhibited an extreme drop before more steadily decreasing with airspeed.

Because we expected the whisker to oscillate near its first mode resonant frequency in response to airflow [19], we computed the power spectrum of the voltage data. However, no obvious resonance was observed.

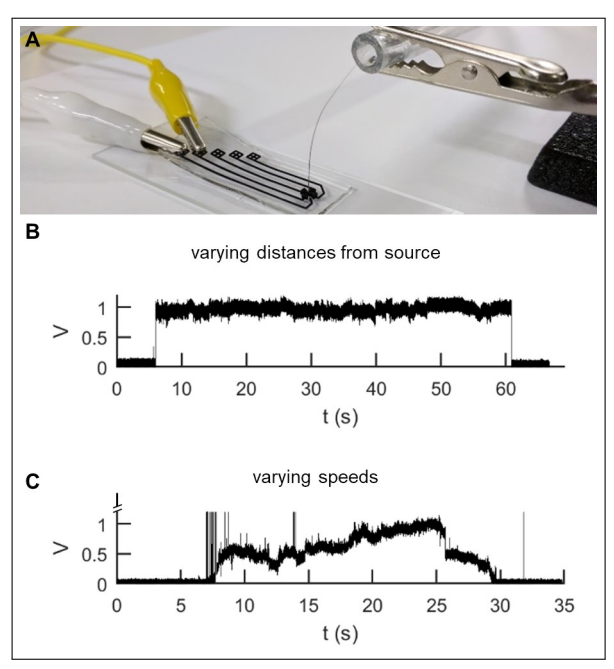


Fig. 6. Response of a single axis of the sensor to airflows of varying distances and speeds. (A) The setup to test the response to airflow includes the sensor, connecting leads, and Tygon tubing. (B) The sensor's response to a constant airflow at two different distances from the whisker ("far-nearfar"). (C) The sensor's response to airflow of varying speed ("up-hold-down"). Airspeed variation was obtained by manually adjusting the pressure valve on the compressed air source. Notice that the y-axis is truncated at $1.2\ V$. Some signals near $7\ s$ and $14\ s$ went up to as high as $3\ V$.

IV. DISCUSSIONS

Future work will focus on improving sensor design to increase its sensitivity and thus extend its application regime:

- Exploration of different geometries may be worthwhile.
 This work explored wedge and pillar shaped pads, but it would be helpful to further parameterize these designs, explore different pillar geometries, and explore different heights between pillars and pads.
- Changes to the fabrication process could improve sensor response. For example, achieving smaller gaps between pillars and pads in the fabrication process could reduce the sensors detection threshold.

- Characterization of the CNT-PDMS composite in the sensing features (pillar and pads) may help to improve the sensor. These features are geometrically "tall" in order to guarantee sufficient contact area for the whisker-to-pillar transmission of mechanics. In empirical observations, the surface of these features is not as consistently conductive as the rest of the sensor. Even though adding sugar powder, as was done for *Material II* in section II-A, ensured satisfactory conductivity on the top surfaces of the sensing features, their side surfaces still lack sufficient conductivity. Possible explanations for different local sensitivities include material inhomogeneities due to gravity and applied pressure.
- To capture whisker vibrations in airflow seems likely to require a sensor with a faster response time and increased, as well as modifications to the circuit board and its connections to reduce electrical noise. One possible approach involves capacitive sensing [2], as it uses the full range between the pillar's resting position and its initial contact with surrounding pads. In addition, recording signals from all four pads instead of only a single pad will more comprehensively capture the whisker's characteristics in response to airflow.

V. CONCLUSION

The present study demonstrated a time- and cost-efficient approach to acquire bending mechanics from a biological whisker. The fabrication process is highly scalable and streamlined for multiple sensors. The flexibility allows mounting to uneven surfaces, such as a 3D-printed model of an animal head. We anticipate using this type of setup to begin to explore coding mechanisms in the tactile neural pathway of the rodent whisker system. Beyond serving the neuroscience research community, we also plan to continue development of artificial whisker-like sensors to explore their broader potential in a variety of engineering applications.

ACKNOWLEDGMENTS

We thank David Collinson for helpful discussions and Hee-Sup Shin for assistance with machining. We thank the Advanced Materials Laboratory at Northwestern University for use of the vacuum chamber and heated press. We thank the Center for Innovation in Global Health Technologies at Northwestern University for use of the FlackTek mixer.

REFERENCES

- [1] Boubenec, Y., Shulz, D., and Debregeas, G. (2012). Whisker encoding of mechanical events during active tactile exploration. Frontiers in Behavioral Neuroscience 6, 74.
- [2] Charalambides, A., and Bergbreiter, S. (2015). A novel all-elastomer MEMS tactile sensor for high dynamic range shear and normal force sensing. Journal of Micromechanics and Microengineering 25, 095009.
- [3] Charalambides, A., and Bergbreiter, S. (2017). Rapid Manufacturing of Mechanoreceptive Skins for Slip Detection in Robotic Grasping. Advanced Materials Technologies 2, 1600188-n/a.
- [4] Chen, H., Miao, L., Su, Z., Song, Y., Han, M., Chen, X., Cheng, X., Chen, D., and Zhang, H.-X. (2017). Fingertip-inspired electronic skin based on triboelectric sliding sensing and porous piezoresistive pressure detection. Nano Energy 40.

- [5] Ebara, S., Kumamoto, K., Matsuura, T., Mazurkiewicz, J.E., and Rice, F.L. (2002). Similarities and differences in the innervation of mystacial vibrissal folliclesinus complexes in the rat and cat: A confocal microscopic study. The Journal of Comparative Neurology 449, 103-119.
- [6] Harada, S., Honda, W., Arie, T., Akita, S., and Takei, K. (2014). Fully Printed, Highly Sensitive Multifunctional Artificial Electronic Whisker Arrays Integrated with Strain and Temperature Sensors. ACS Nano 8, 3921-3927.
- [7] Hibbeler, R.C. (2014). Mechanics of Materials, 9th edn (Boston: Prentice Hall).
- [8] Hires, S.A., Schuyler, A., Sy, J., Huang, V., Wyche, I., Wang, X., and Golomb, D. (2016). Beyond cones: an improved model of whisker bending based on measured mechanics and tapering. Journal of Neurophysiology 116, 812-824.
- [9] Huet, L.A., Rudnicki, J.W., and Hartmann, M.J.Z. (2017). Tactile Sensing with Whiskers of Various Shapes: Determining the Three-Dimensional Location of Object Contact Based on Mechanical Signals at the Whisker Base. Soft Robotics 4, 88-102.
- [10] Huet, L.A., Schroeder, C.L., and Hartmann, M.J.Z. (2015). Tactile signals transmitted by the vibrissa during active whisking behavior. Journal of Neurophysiology 113, 3511-3518.
- [11] Johnston, I.D., McCluskey, D.K., Tan, C.K.L., and Tracey, M.C. (2014). Mechanical characterization of bulk Sylgard 184 for microfluidics and microengineering. Journal of Micromechanics and Microengineering 24, 035017.
- [12] Li, Q., Li, J., Tran, D., Luo, C., Gao, Y., Yu, C., and Xuan, F. (2017). Engineering of carbon nanotube/polydimethylsiloxane nanocomposites with enhanced sensitivity for wearable motion sensors. Journal of Materials Chemistry C 5, 11092-11099.
- [13] Quist, B.W., Faruqi, R.A., and Hartmann, M.J.Z. Variation in Young's modulus along the length of a rat vibrissa. Journal of Biomechanics 44, 2775-2781.
- [14] Quist, B.W., Seghete, V., Huet, L.A., Murphey, T.D., and Hartmann, M.J.Z. (2014). Modeling Forces and Moments at the Base of a Rat Vibrissa during Noncontact Whisking and Whisking against an Object. The Journal of Neuroscience 34, 9828.
- [15] Vaxenburg, R., Wyche, I., Svoboda, K., Efros, A.L., and Hires, S.A. (2018). Dynamic cues for whisker-based object localization: An analytical solution to vibration during active whisker touch. PLOS Computational Biology 14, e1006032.
- [16] Yan, W., Kan, Q., Kergrene, K., Kang, G., Feng, X.-Q., and Rajan, R. (2013). A truncated conical beam model for analysis of the vibration of rat whiskers. Journal of Biomechanics 46, 1987-1995.
- [17] Yang, A.E.T., and Hartmann, M.J.Z. (2016). Whisking Kinematics Enables Object Localization in Head-Centered Coordinates Based on Tactile Information from a Single Vibrissa. Frontiers in Behavioral Neuroscience 10.
- [18] Yu, Y.S.W., Graff, M.M., Bresee, C.S., Man, Y.B., and Hartmann, M.J.Z. (2016). Whiskers aid anemotaxis in rats. Science Advances 2, e1600716.
- [19] Yu, Y.S.W., Graff, M.M., and Hartmann, M.J.Z. (2016). Mechanical responses of rat vibrissae to airflow. The Journal of Experimental Biology 219, 937.